# Gravity Waves Appearing in a High-Resolution GCM Simulation

KAORU SATO

*Department of Geophysics, Faculty of Science, Kyoto University, Kyoto, Japan*

TOSHIRO KUMAKURA

*Department of Civil and Environmental Engineering, Nagaoka University of Technology, Nagaoka, Japan*

MASAAKI TAKAHASHI

*Center for Climate System Research, University of Tokyo, Tokyo, Japan*

(Manuscript received 5 August 1997, in final form 10 April 1998)

ABSTRACT

Global characteristics of gravity waves in the lower stratosphere are examined using a GCM with high resolution in both the horizontal (T106, corresponding to about 120 km) and the vertical (~600 m). The bottom boundary condition of the model is that of an aquaplanet with perpetual February sea surface temperature. The simulated gravity waves are in good agreement with mesosphere–stratosphere–troposphere (MST) radar observations at a middle latitude on the gravity wave structure and on the frequency spectra as a function of height. The frequency spectra of simulated wind and temperature fluctuations are also examined as a function of latitude. Large values of spectral density are observed at frequencies higher than the inertial frequency ($f$) in a weak wind region around 20 km, which is consistent with the characteristics of internal gravity waves. An isolated peak is observed near $f$ for horizontal wind spectra at latitudes higher than 10°, while the energy is distributed in a wide range of frequency at lower latitudes where $f$ approaches zero.

Further analysis is performed of those fluctuations having periods shorter than 24 h and those having vertical wavelengths smaller than 5 km. These are frequently analyzed as gravity waves using observation data. The distribution of energy and momentum fluxes in the latitude–height section is examined. The result indicates that short-period waves mostly propagate upward and poleward from the equatorial region. The wave energy reaches about 50° lat at the 27-km altitude. A negative (positive) maximum of vertical flux of meridional momentum ($\overline{v'w'}$) is seen above the subtropical jet in the Northern (Southern) Hemisphere for small vertical-scale gravity waves. This is consistent with the preferred equatorward propagation of the wave indicated by a statistical analysis based on MST radar observations. The ratio of potential to kinetic energy maximizes over the equator and decreases poleward. The Eliassen–Palm flux divergence associated with gravity waves is decelerative above the subtropical jet, albeit small.

## 1. Introduction

Since the role of gravity waves on the maintenance of closing of mesospheric jets was discussed theoretically at the beginning of the 1980s (Lindzen 1981; Matsuno 1982), we have come to recognize the importance of gravity waves in the global circulation of the middle atmosphere through numerous observational and theoretical studies. The drag due to topographically forced gravity waves has been included in the general circulation model (GCM) and numerical prediction model to simulate a realistic weak wind layer in the lower stratosphere through various parameterizations (Palmer et al. 1986; McFarlane 1987; Iwasaki et al. 1989). The theoretically estimated momentum flux convergence to maintain these weak wind layers was confirmed qualitatively by mesosphere–stratosphere–troposphere (MST) radar observations, which provided accurate estimates of momentum fluxes (e.g., Tsuda et al. 1990; Sato 1994).

Recent studies are focusing on the role of nonstationary gravity waves that may be generated or associated with convection, jet stream, synoptic-scale waves, frontal system, etc. According to recent theoretical and observational studies, momentum fluxes of planetary-scale equatorial Kelvin and Rossby–gravity waves are insufficient to drive the quasi-biennial oscillation (QBO) in the equatorial lower stratosphere. It may perhaps be natural to consider gravity waves as the main driving

*Corresponding author address:* Dr. Kaora Sato, Department of Geophysics, Faculty of Science, Kyoto University, Kyoto 606-8502, Japan.
E-mail: sato@kugi.kyoto-u.ac.jp

agents of the QBO (see Dunkerton 1997, for a review). A QBO-like (about 1.5 yr) oscillation has recently been simulated by Takahashi (1996) using a GCM with fine vertical grids to resolve the fine vertical structures observed in winds and temperature, which are probably mostly due to gravity waves. His model horizontal resolution is, however, not very high (T21). Horinouchi and Yoden (1998) also succeeded in simulating the QBO-like (about 400 days) oscillation in a GCM (T42) with latitudinally independent SST. They noted the importance of gravity waves. On the other hand, Alexander and Rosenlof (1996) found that the gravity wave–induced force is accelerative in the extratropical summer stratosphere above 20 km by using a linear model to calculate the propagation of gravity wave spectra through climatological mean winds. They also suggested the importance of nonstationary gravity waves.

It is important, therefore, to examine the characteristics of nonstationary and stationary gravity waves at all latitudes. There have been several efforts to understand the global distribution of gravity waves using observational data from radiosondes for the lower stratosphere (Kitamura and Hirota 1989; Allen and Vincent 1995), and rockets (Hirota 1984; Eckermann et al. 1995) and satellites (Fetzer and Gille 1994; Wu and Waters 1996) for the stratosphere and mesosphere. However, these observational tools provide information for only a limited range of gravity waves that are intrinsically distributed in a wide spectral range of vertical [$O$(0.1 km) to $O$(10 km)] and horizontal wavelengths [$O$(1 km) to $O$(1000 km)], and frequencies [$O$(1 min) to $O$(10 h) in the midlatitude region] (e.g., Alexander 1998). Moreover, it is usually impossible to observe all physical quantities simultaneously. Thus, we usually need to make some assumption to obtain the total energy or momentum fluxes of gravity waves from observational data.

With the aid of ever-developing computer technology, it is becoming possible to integrate GCMs and resolve gravity waves explicitly (e.g., Hayashi et al. 1989; Hamilton 1996; Hayashi et al. 1997). O'Sullivan and Dunkerton (1995) showed inertia-gravity waves having large amplitudes embedded in a life cycle of baroclinic waves using a dry three-dimensional primitive equation model (T126). They emphasized the importance of vertical resolution to simulate gravity waves with short wavelengths approaching their critical levels and adopted 700 m for vertical grid spacing. Recently, Jones et al. (1997) examined the effect of increasing horizontal resolution in a GCM (Geophysical Fluid Dynamics Laboratory SKYHI model) from about 100 to 60 km on the global circulation. However, the vertical resolution of their GCM may be too coarse (40 levels from the ground to the mesopause) to resolve observed gravity waves with short vertical wavelengths. For example, typical vertical wavelengths of gravity waves are 1–4 km in the lower stratosphere (Sato 1994; Sato et al. 1997).

In this study, we use a GCM with high resolution both in the horizontal and vertical directions to examine global statistical characteristics of gravity waves in the lower stratosphere. A description of the model is given in section 2, and the simulated mean fields are shown in section 3. The realistic features of the simulated waves will be confirmed by comparison with observational data in section 4. Detailed characteristics of gravity waves are shown in section 5 in terms of frequency spectra as a function of latitude (section 5a) and global distribution of energy and momentum fluxes in the latitude–height sections (section 5b). Results are discussed in section 6. Summary and concluding remarks are made in section 7.

## 2. Model description and experiments

The model is the first version of the atmospheric GCM developed at the Center for Climate System Research/National Institute for Environmental Studies (CCSR/NIES). Basic features of the model can be found in Numaguti (1993). Newly implemented physical processes are discussed in Numaguti et al. (1995). A detailed description of the radiation scheme can be found in Nakajima et al. (1995).

The horizontal resolution is T106, corresponding to a grid spacing of about 120 km. There are 53 layers in the vertical, having about a 600-m vertical resolution in the upper troposphere and lower stratosphere. The top level of the model is located at about 0.5 hPa (approximately 50 km, the 0.0005 sigma level).

Following previous QBO-like simulation by the CCSR/NIES GCM (Takahashi 1996; Takahashi et al. 1997), a moist convective adjustment scheme is used as the cumulus parameterization in this experiment, although the standard convection scheme of the CCSR/NIES GCM is the prognostic Arakawa–Schubert scheme (Numaguti et al. 1995). The Mellor–Yamada level-2 closure scheme is used as the vertical eddy viscosity in the free atmosphere as well as in the bottom boundary layer in which the minimum vertical eddy viscosity coefficient is set to 0.15 $m^2 s^{-1}$. A fourth-order horizontal diffusion with a damping time of 0.2 day at the maximum wavenumber is applied. In addition, the dry convective adjustment scheme is used in the stratosphere to represent wavebreaking. Near the top boundary, a Rayleigh friction is used with a coefficient $\alpha$ as a function of height $z$:

$$\alpha(z) = \alpha_0 \max\left[10^{-20}, 1 + \tanh\left(\frac{z - z_{\text{top}}}{z_d}\right)\right], \quad (1)$$

where $\alpha_0$ is $(1/7 \text{ day})^{-1}$, $z_{\text{top}} \sim 50$ km, and $z_d = 7$ km.

The bottom boundary condition is that of an aquaplanet (an idealistic moist atmosphere on a sphere covered only by the ocean). Values of sea surface temperature (SST) climatology in February are given independent of longitude and time (perpetual February). There is a diurnal cycle in the solar forcing. The other

processes and schemes are the same as those in the standard CCSR/NIES GCM.

As for the start-up run, a horizontal resolution T21, 53-layer (T21L53) model of the same boundary condition was integrated with an initial condition of an isothermal atmosphere at rest over 120 model days to obtain a quasi-steady state. The final day of T21L53 model simulation was used as the initial condition for the T106L53 model. The T106L53 model was run for 80 days and obtained a quasi-steady state.

The final 20 days of the run, output at a 1-h interval, were used for the analysis of gravity wave activities. To avoid aliasing from fluctuations of higher frequencies, values averaged over 1-h were used. Thus, gravity waves having wave periods longer than about 2 h are included in the analyzed data. Data were interpolated by a spline method in the vertical to fixed points in the log-pressure vertical coordinate having almost the same vertical spacing in the original sigma coordinate. The vertical wind velocity $w$ is obtained using the following formula:

$$w \sim H\left(\frac{d\ \ln\sigma}{dt} + \frac{d\ \ln P_s}{dt}\right), \qquad (2)$$

where $H$ is a scale height (taken to be 7 km) and $P_s$ is the surface pressure.

## 3. Mean field

The zonal- and time-averaged zonal wind $U$ is plotted in Fig. 1a. The subtropical westerly jet is situated around 32°N and 45°S, with peak values larger than 40 and 30 m s$^{-1}$, respectively. The position and strength are both realistic. The polar night jet is too strong compared to the real atmosphere (i.e., Northern Hemisphere in February) probably because of the absence of stationary waves caused by topography. The jet strength is, however, comparable to the polar night jet in the Southern Hemisphere in July. The axis of the polar night jet is around 60°N as in the real atmosphere. The polar night jet and subtropical jet are clearly separated in the Northern Hemisphere.

Compared with a low resolution version of our GCM, the mean zonal wind field is significantly improved in the equatorial troposphere. A westerly bias in this region was observed in the T21 CCSR/NIES model with which Takahashi (1996) succeeded in simulating the QBO-like feature in the equatorial lower stratosphere. The westerly bias is absent in our present T106 model and realistic easterlies are simulated.

Figure 1b shows the latitude–height section of the Brunt–Väisälä frequency squared ($N^2$). The tropopause height, with large $N^2$ vertical gradient, is 15–17 km in the tropical region and about 8–10 km in the middle and high latitude regions. We will use the curve of 2.5 $\times$ 10$^{-4}$ (s$^{-2}$) as an indicator of the tropopause in the following figures. It should be noted that although this curve indicates appropriate tropopause levels at the middle and high latitudes, it traces levels lower than the tropical tropopause in the model by 1–2 km.

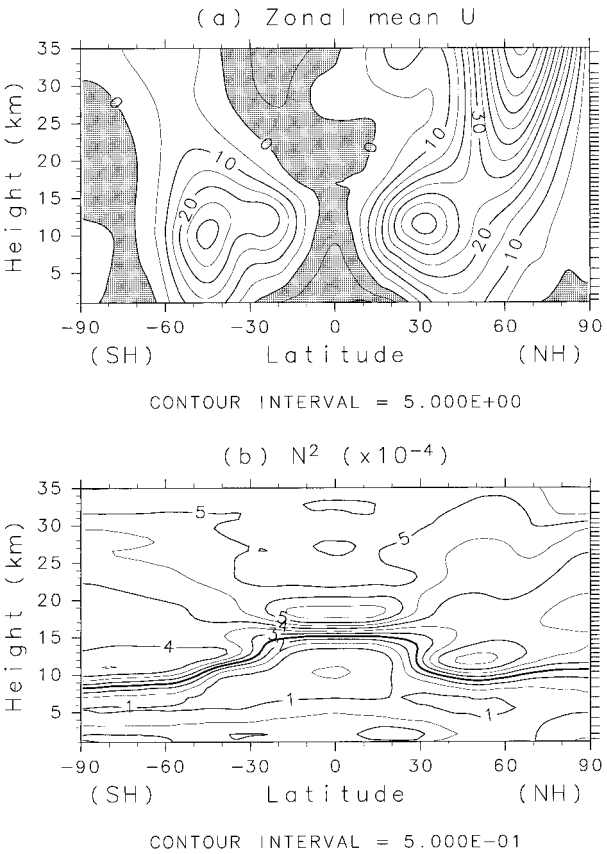


FIG. 1. (a) Latitude–height cross section of zonal-mean zonal wind averaged over 20 days. Contour intervals are 5 m s$^{-1}$. Easterly regions are shaded. (b) Latitude–height cross section of Brunt–Väisälä frequency squared. Contour intervals are 5 $\times$ 10$^{-5}$ s$^{-1}$. A thick contour denotes 2.5 $\times$ 10$^{-4}$ s$^{-1}$, roughly corresponding to the tropopause level. Tick marks on the right axis indicate model vertical grid positions.

## 4. Comparison with MST radar observations

To see how realistic the simulated gravity wave field is, we made a comparison with observational data. Figures 2a and 2b show the time–height sections of zonal ($u$) and meridional winds ($v$) obtained through a special long-term (19 days) continuous observation with the middle and upper (MU) atmosphere radar, which is an MST radar located at Shigaraki, Japan (35°N, 136°E). See Fukao et al. (1985) for details of the MU radar. Although the observation was conducted in April 1995, the gravity wave field may be comparable with that in the model because the subtropical jet, one of the gravity wave sources, is strong even in this season over Japan.

A clear downward-propagating phase structure is observed in both $u$ and $v$ profiles in the 19–25-km height region (see contours of 0 or 10 m s$^{-1}$), where the zonal-mean wind is very weak. The vertical wavelength and

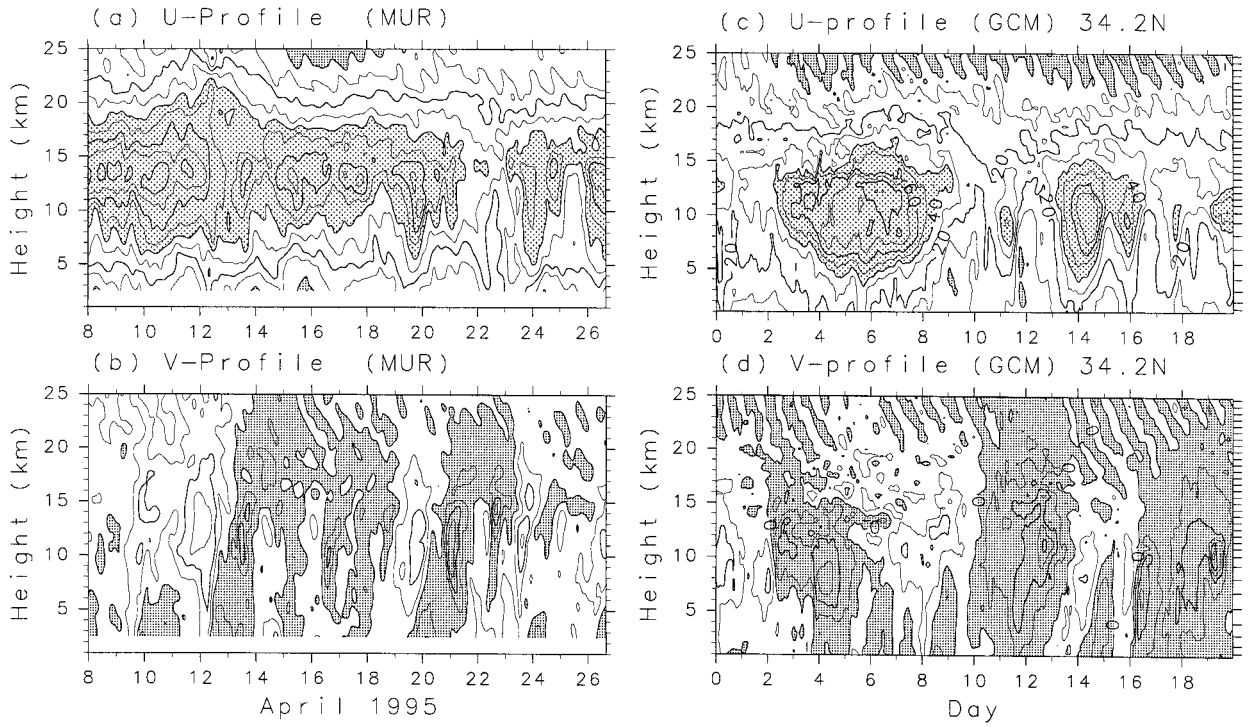


FIG. 2. Time–height sections of (a) $u$ and (b) $v$ observed with the MU radar (35°N, 136°E) over 19 days in April 1996, and (c) $u$ and (d) $v$ at 34.2°N simulated by the GCM over 20 days. Negative regions are darkly shaded. Lightly shaded are the regions where $u > 40$ m s$^{-1}$. Contour intervals are 10 m s$^{-1}$.

wave period are about 3.5 km and 20 h, respectively. Sato et al. (1997) showed that the wave structure is due to inertia–gravity waves of horizontal wavelength of about 1200 km, propagating westward with a phase speed of about 10 m s$^{-1}$. The vertical and horizontal wavelengths are sufficiently large to be resolved in our high-resolution model.

Figures 2c and 2d show time–height sections of simulated $u$ and $v$ at the latitude of 34.2°N over 20 days. The tick marks on the right indicate the model's vertical grids. The height position (about 11–12 km) and strength of the subtropical jet in simulated $u$ are similar to observation. The westward tilt with height of baroclinic wave phase structure should be observed as delay with height in the time–height section. The tilt of zero contours of the simulated $v$ (e.g., day 10 and day 16) is similar to that of radar observation (e.g., 12 and 20 April), indicating that the simulated baroclinic waves are realistic. The most important feature in Figs. 2c and 2d is that gravity wave structure having a vertical wavelength and a wave period similar to observation (Figs. 2a and 2b) is seen in the lower stratosphere of the model. Similar features are observed at other longitudes.

Power spectra versus ground-based frequency are shown in Figs. 3a and 3b for the observed and simulated $v$, respectively, as a function of height. The simulated spectra are averaged over eight longitudes including those shown in Fig. 2d. The chosen eight longitudes are mentioned at the beginning of the next section. A thick solid vertical line in each figure indicates the inertial frequency (~20 h) and two thick dashed vertical lines show the periods of one day and a half-day. There are peaks corresponding to baroclinic waves with about a 4-day period around a 10-km height and near the ground in both spectra. However, the peak near the ground is weaker in the simulated spectra probably because of the aquaplanet boundary condition.

The inertia–gravity waves in the weak wind layer above 17 km in the lower stratosphere are observed as an isolated peak around the inertial period both in observed and simulated spectra. The peak values are almost the same (~20 km). It is worth noting that the isolated peak in simulated spectra continues at greater height where there are no observations.

Therefore, the inertia-gravity waves in the model are very similar to the observation in terms of amplitudes, vertical wavelengths, and periods. This result is very encouraging and suggests that the simulated gravity wave field in our model is fairly realistic.

## 5. Statistical characteristics of gravity waves

The 20-day model dataset at 1-h time interval is so large that it is not feasible to analyze every longitude. Since there is no longitudinal dependence on a boundary condition in the present model, the statistical characteristics of gravity waves must be independent of longitude. Thus, in the following sections we analyze time

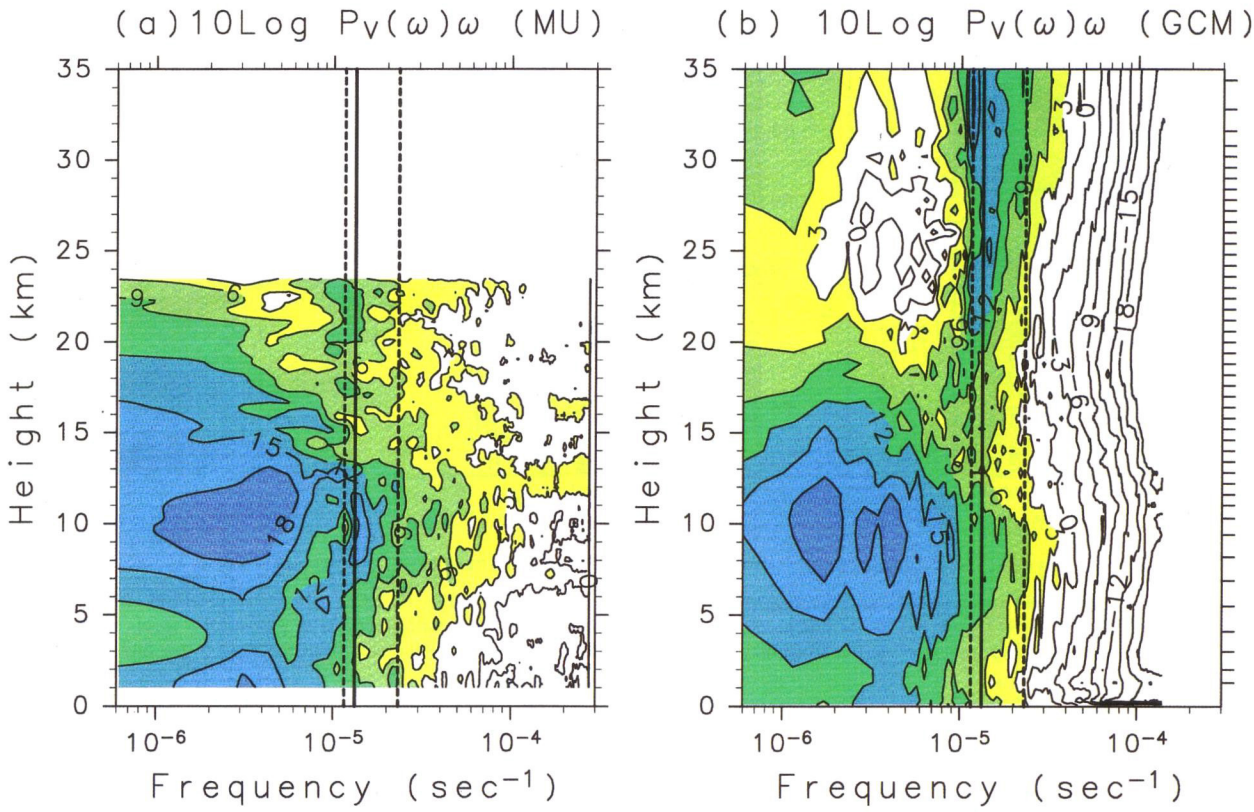


FIG. 3. Frequency power spectra in the energy-content form of $v$ fluctuations $[P_v(\omega)\omega]$ as a function of height for (a) MU radar observations at 35°N and (b) GCM simulations at 34.2°N. The units of the power spectra are $m^2\ s^{-2}$. Contours are drawn for 10 log $P_v(\omega)\omega$ with intervals of 3 dB. A thick solid line indicates inertial frequency (~21 h). Two dashed lines indicate frequencies of 1 day and a half day.

series of eight longitudes with the same longitudinal interval (45°) and examine the average as the statistics of the model.

### *a. Spectral characteristics as a function of latitude*

Frequency power spectra were calculated at each of eight longitudes as a function of latitude ($\phi$) and height ($z$), and the average of eight spectra was obtained. The spectra were further averaged for the height regions of 12–17 km, 17–22 km, and 22–27 km with fine vertical resolution. Results for $v$ are shown in Fig. 4. Thick solid curves indicate the inertial frequency at each latitude and dashed curves indicate the periods of one day and a half day.

Large values are distributed at higher frequency regions enclosed equatorward by the curve of the inertial frequency, particularly in upper regions. The ground-based wave frequency is considered to almost equal the intrinsic frequency in the upper region because the mean wind is weak there except at the latitudes around the polar night jet (~60°N). Thus, this spectral feature is consistent with the theory of internal gravity waves that their intrinsic frequencies should be higher than the inertial frequency. An interesting feature is that isolated peaks are observed around the inertial frequency at each latitude up to $\phi = \pm 45°$ in the 17–22-km region and up to $\phi = \pm 55°$ in the 22–27-km region, except around the equator. The spectra around the equator are widely distributed and no particular peaks are observed.

The spectra around the subtropical jet ($\phi = \pm 30°$ for 12–17 km) and polar night jet ($\phi = 60°$N for 22–27 km) seem spread at frequencies lower than the inertial frequency because of the Doppler effect of strong mean wind. In the 12–17-km height region, the spectral values at frequencies higher than a half day are maximized meridionally around the equator and around $\phi = \pm 30°$ where the subtropical jet is situated. The maxima around $\phi = \pm 30°$ disappear at higher regions.

The power spectra for $u$, vertical wind $w$, and potential temperature $\theta$ are shown in Fig. 5. Characteristics of $u$ are similar to those of $v$. The $w$ spectra are widely distributed at higher frequencies compared with $u$ and $v$. Potential temperature spectra are also spread widely, but the frequency region with large values is similar to $u$ and $v$ spectra.

### *b. Global energy distribution and meridional propagation of gravity waves*

It is generally difficult to extract gravity wave components with only time filters because the wave fre-

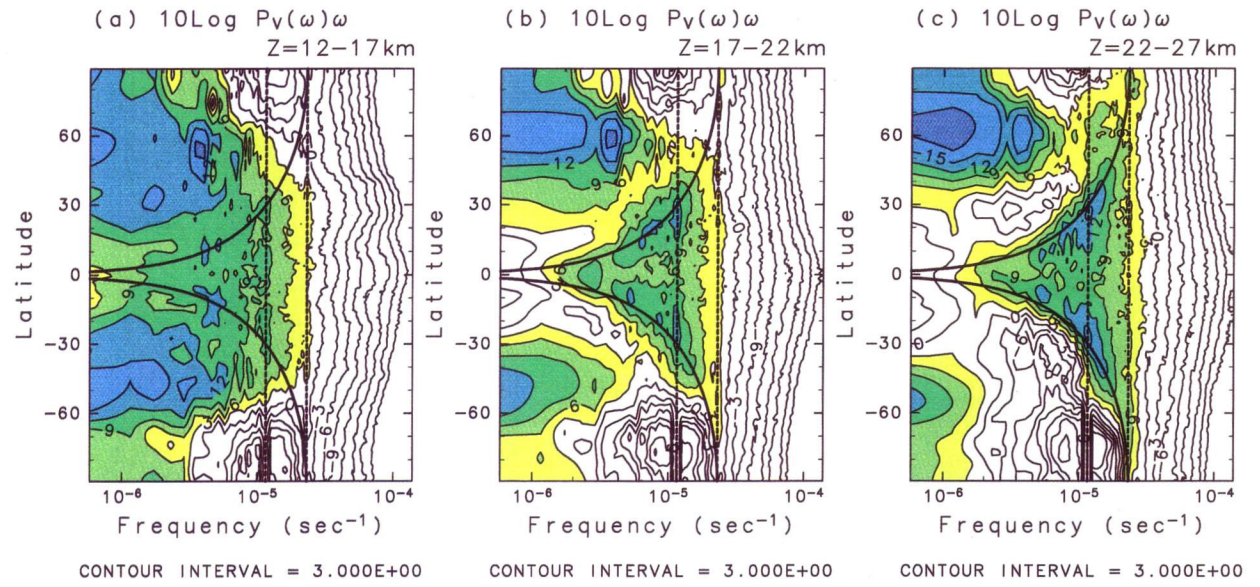


FIG. 4. Frequency power spectra in the energy-content form of $v$ fluctuations simulated by GCM as a function of latitude for the height regions of (a) 12–17, (b) 17–22, and (c) 22–27 km. Contours are drawn for 10 log $P_v(\omega)\omega$ with intervals of 3 dB. Color levels are the same as Fig. 3. A thick solid curve indicates inertial frequency at each latitude. Two dashed lines indicate frequencies of 1 day and a half day.

quency can be Doppler-shifted by a strong mean wind. An extreme is topographically forced waves having zero frequency. The identification of gravity waves by their small vertical scales is also difficult, particularly in the equatorial regions where equatorial Kelvin and Rossby–gravity waves can also have short vertical wavelengths. Inertial instability with fine vertical structures can also occur in the equatorial regions. Small vertical-scale motions other than gravity waves in the Northern Hemisphere (winter) may exist within the surf zone of Rossby waves (e.g., Haynes and Anglade 1997). However, the Rossby wave activity in the model is probably weaker than in the real atmosphere because there are no continents in our model.

Here we examine two kinds of wave fluctuations, which are frequently treated as gravity waves in observational studies: short-period waves and small vertical-scale waves. The former is used for analysis of the time

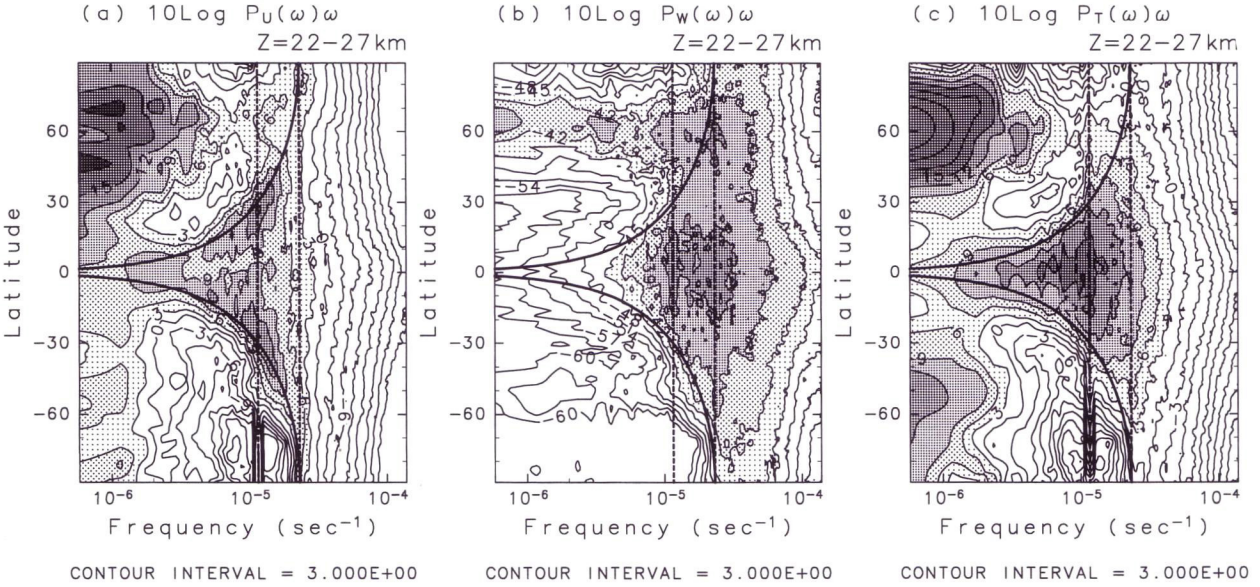


FIG. 5. The same as Fig. 4 but for (a) $u$, (b) $w$, and (c) $\theta$ fluctuations in the height region of 22–27 km. Units of the power spectra are $m^2\ s^{-2}$ for (a) and (b) and $K^2$ for (c). Contour intervals are 3 dB. A thick solid curve indicates inertial frequency at each latitude. Two dashed lines indicate frequencies of 1 day and a half day.

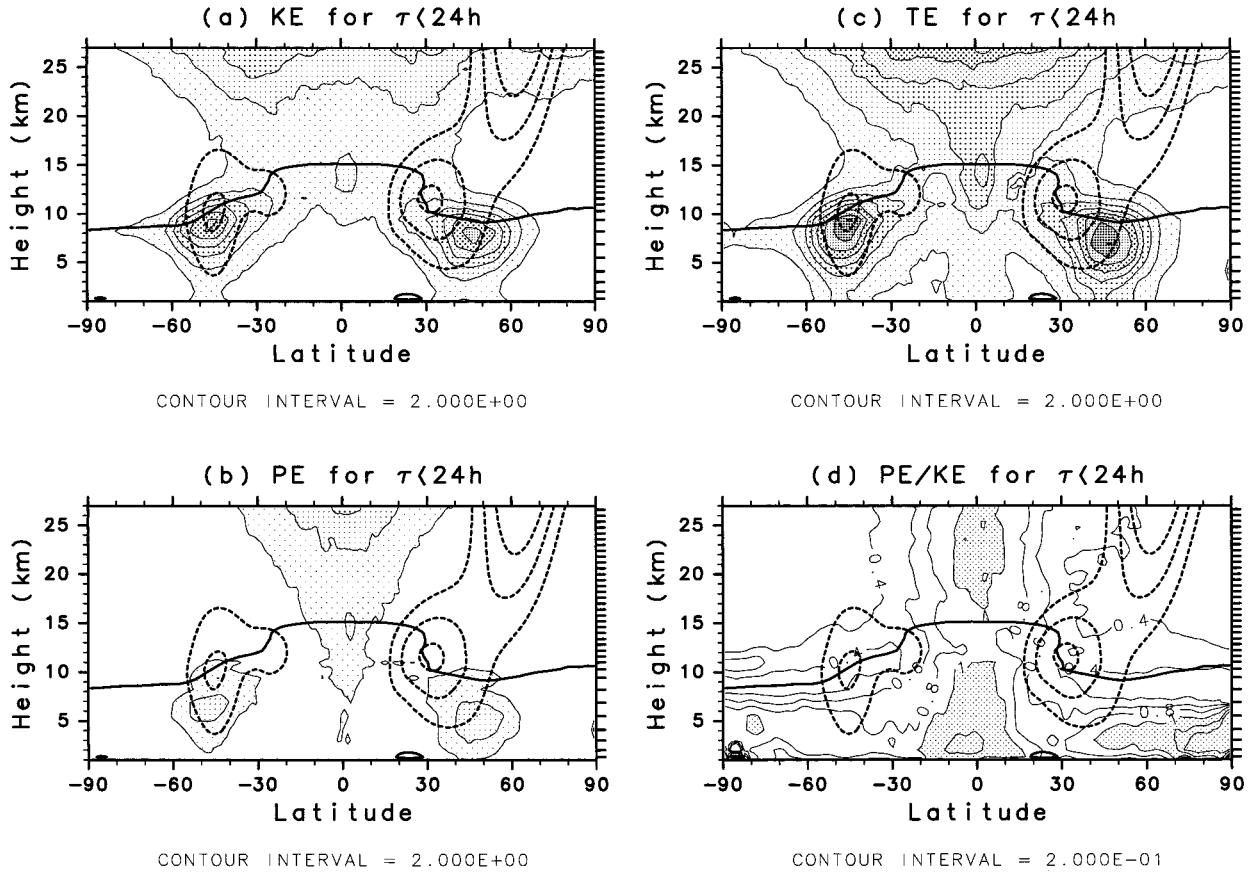


FIG. 6. Latitude–height sections of (a) kinetic energy, (b) potential energy, (c) total energy, and (d) ratio of potential to kinetic energy of short-period gravity waves. Contour intervals are 2 $m^2 s^{-2}$ for (a), (b), and (c). Contours in (d) are drawn for 0.2, 0.4, 0.6, 0.8, 1, 1.5, and 2. The regions with energy larger than 2 $m^2 s^{-2}$ for (a), (b), and (c) are shaded. Regions with the ratio larger than 1 are shaded for (d).

series data from measurements with fine temporal resolution such as MST radars. The latter is used for observations with fine vertical resolution such as radiosondes. In the following, the wave characteristics are discussed in the height region up to 27 km where fine vertical structures are resolved in the model.

### 1) SHORT-PERIOD GRAVITY WAVES

To extract short-period components, we applied a high-pass filter with a cutoff period of 1 day to the model data. The wave period does not change significantly during propagation when the mean field is almost steady, whereas the vertical wavelength changes according to the mean field such as $U$ and $N^2$.

Kinetic [KE $\equiv \frac{1}{2}(\overline{u'^2} + \overline{v'^2} + \overline{w'^2})$], potential [PE $\equiv \frac{1}{2}(g^2/N^2)(\overline{\theta'^2}/\overline{\theta}^2)$], and total (TE $\equiv$ KE + PE) energies divided by atmospheric density for short-period waves are plotted in Fig. 6. A thick solid curve in each figure indicates the tropopause (see section 3) and thick dashed curves are contours of $U$ at 20, 30, and 40 m $s^{-1}$.

In the lower stratosphere above 15 km, both KE and PE increases as altitude increases, mostly due to decrease of atmospheric density. The latitudinal extent is larger for KE than PE. The maximum of KE is observed around $|\phi| = 20°$–$30°$ in both hemispheres, whereas the PE is maximized over the equator. As the result, TE is widely distributed over the equator. Another weak maximum is observed in KE around 70°N, north of the polar night jet axis.

There are maxima over the equator and at $\phi = \pm 45°$ below the tropopause in both hemispheres. Although these maxima may be partly due to gravity waves, there is a possibility of mesoscale phenomena such as convection and fronts. Thus, further discussion is not made for the troposphere.

Figure 6d shows the ratio $R$ of PE to KE. The regions with $R$ larger than 1 are shaded. Note that $R$ is almost unity over the equator and decreases as latitude increases. For inertia–gravity waves in an $f$ plane, the ratio $R$ is expressed as

$$R = \left(\frac{2f^2}{N^2}\frac{m^2}{k^2} + 1\right)^{-1}, \tag{3}$$

where $f$ is the inertial frequency and $m$ and $k$ are vertical and horizontal wavenumbers, respectively (Gill 1982). Thus, $R$ should be 1 for $f = 0$ at the equator and be

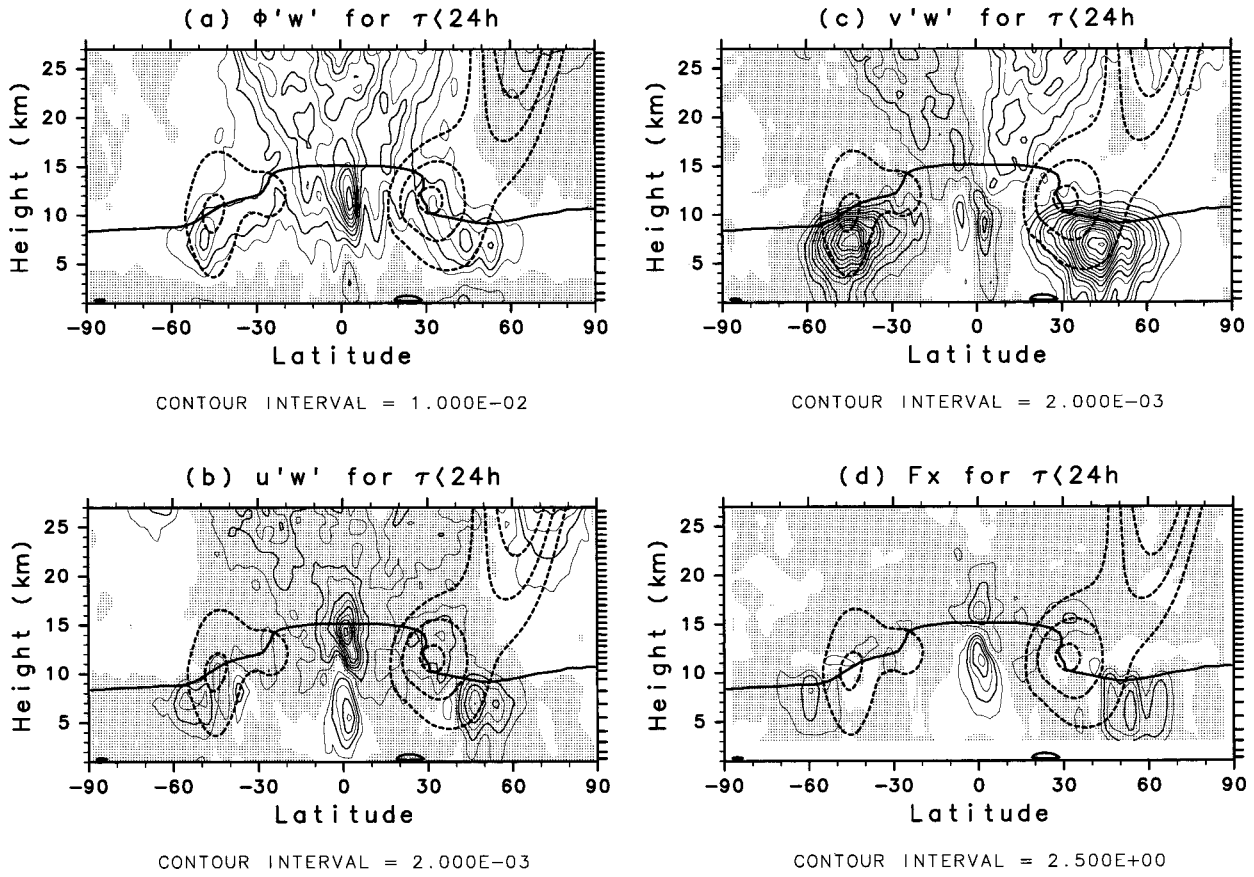


FIG. 7. Latitude–height sections of vertical fluxes of (a) energy ($\overline{\Phi' w'}$), (b) zonal momentum ($\overline{u'w'}$), (c) meridional momentum ($\overline{v'w'}$), and (d) EP flux divergence ($F_x$) for short-period gravity waves. Contour intervals are 0.01 m$^2$ s$^{-1}$ for (a), 0.002 m$^2$ s$^{-2}$ for (b) and (c), and 2.5 m s$^{-1}$/month for (d). Negative regions are shaded.

smaller than 1 for higher latitudes, as observed in Fig. 6d. If the typical aspect ratio $k/m$ of inertia–gravity waves is independent of latitude, $R$ decreases with $f$. The monotonic decrease of $R$ with latitude observed in Fig. 6d may be due to the increase of $f$ with latitude.

The momentum fluxes are useful values to examine the horizontal propagation of internal gravity waves. Positive (negative) $\overline{u'w'}$ means eastward (westward) propagation and positive (negative) $\overline{v'w'}$ means northward (southward) propagation relative to the mean wind for gravity waves propagating energy upward. The signs are reversed for downward energy propagation. Note that for internal gravity waves, the horizontal directions of phase and energy propagation relative to the mean wind are the same, while the vertical directions are opposite. Moreover, the momentum fluxes $\rho_0\overline{u'w'}$ and $\rho_0\overline{v'w'}$ ($\rho_0$ is atmospheric density) are invariant for conservative waves. The vertical energy propagation can be examined from vertical energy flux.

Figure 7a shows the vertical energy flux $\overline{\Phi' w'}$ associated with short-period waves, where $\Phi'$ is the geopotential height fluctuation component. The energy flux is mostly positive in the lower stratosphere in the low-latitude region ($|\phi| < 50°$), indicating dominance of upward energy propagation. Negative values meaning downward energy propagation are observed around the polar night jet. This point will be discussed in section 6.

Figures 7b and 7c show $\overline{u'w'}$ and $\overline{v'w'}$, respectively. In the low-latitude region ($|\phi| < 50°$) where energy flux is upward, $\overline{u'w'}$ are negative, indicating that the gravity waves propagate westward relative to the mean wind. The order of magnitude $O(10^{-3})$ m$^2$ s$^{-2}$ is comparable to net $\overline{u'w'}$ estimates from radiosonde observation data at Singapore (1.4°N, 104.0°E) for short-period (<3 days) components by Sato and Dunkerton (1997). The characteristics of $\overline{v'w'}$ there are interesting. Negative (positive) values are observed in the Southern (Northern) Hemisphere. Moreover, the latitudinal expanse of large $\overline{v'w'}$ and $\overline{u'w'}$ increases with altitude. The $\overline{v'w'}$ contours of $\pm 2 \times 10^{-3}$ m$^2$ s$^{-2}$ reach the midlatitude of $\phi = \pm 50°$ at $z = 27$ km. This V-shaped distribution suggests that short-period gravity waves are generated in the equatorial region and propagate poleward in both hemispheres. Similar poleward propagation was suggested by Manzini and Hamilton (1993), who analyzed vertical Eliassen–Palm (EP) flux associated with small

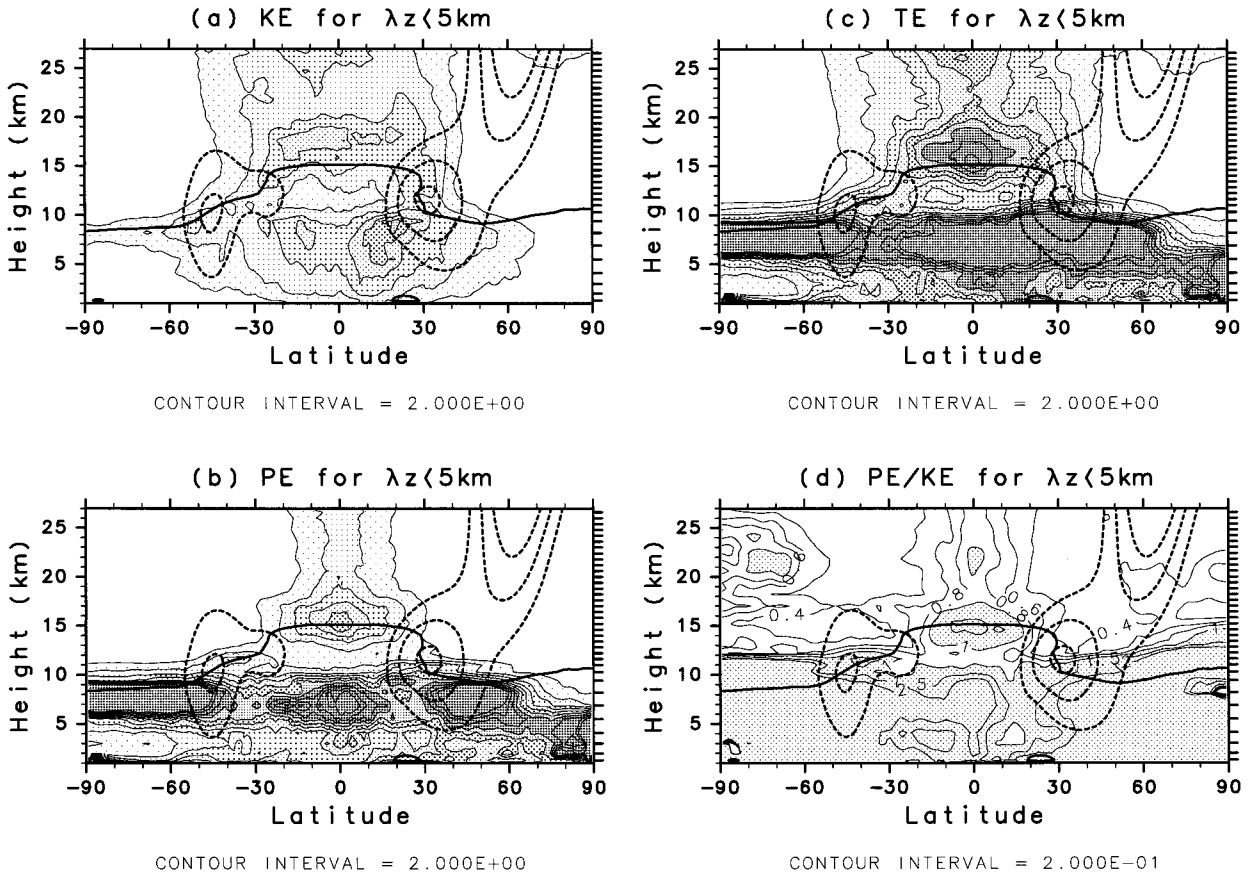


FIG. 8. The same as Fig. 6 but for small vertical-scale gravity waves.

zonal-scale waves in the GFDL SKYHI model and a linear model.

The effect of short-period gravity waves on the mean wind circulation is examined by calculating the EP flux defined as

$$\mathbf{F} = (F^{(\phi)}, F^{(z)}), \tag{4}$$

$$F^{(\phi)} = \rho_0 a \cos\phi \left( \frac{\overline{u}_z}{\overline{\theta}_z} \overline{v'\theta'} - \overline{v'u'} \right), \quad \text{and} \tag{5}$$

$$F^{(z)} = \rho_0 a \cos\phi \left\{ \left[ f - \frac{(\overline{u}\cos\phi)_\phi}{a\cos\phi} \right] \frac{1}{\overline{\theta}_z} \overline{v'\theta'} - \overline{u'w'} \right\}, \tag{6}$$

and its divergence as the wave-driven force $F_x$ is

$$F_x = (a\cos\phi)^{-1} \frac{\partial}{\partial\phi}(F^{(\phi)}\cos\phi) + \frac{\partial F^{(z)}}{\partial z}, \tag{7}$$

where $a$ is a mean radius of the earth and the subscript $z$ denotes a vertical derivative (Andrews et al. 1987). The result for $F_x$ is shown in Fig. 7d. A westward force with a maximum of 5 m s$^{-1}$ month$^{-1}$ is observed in the upper part of the subtropical westerly jet around 30°N. The $F_x$ contour of 2.5 m s$^{-1}$ month$^{-1}$ shows that the latitudinal and height expanse of the forced region is 20° and 3 km, respectively. The westward force is smaller by one order of magnitude compared with the drag due to topographically forced gravity waves (e.g., Palmer et al. 1986; McFarlane 1987).

### 2) SMALL VERTICAL-SCALE GRAVITY WAVES

Small vertical-scale gravity waves are extracted from original model data by applying a digital highpass filter to the vertical profiles with a cutoff length of eight grids. The cutoff length corresponds to a wavelength of about 5 km in the upper troposphere and lower stratosphere, where the grid spacing is fine and where gravity wave characteristics are discussed in this section.

Figure 8 shows latitude–height sections of KE, PE, TE, and $R$ for small vertical-scale gravity waves. There are several characteristics different from those of short-period gravity waves. For example, KE is maximized at 3 km above the equatorial tropopause over the latitudinal expanse of ±30°. Another region with large KE is above the subtropical jet around 30°N in the Northern Hemisphere, where both tropical (~16 km) and extratropical tropopauses (~9 km) exist. This makes KE distribution asymmetric around the equator. On the other hand, PE is maximized around the tropical tropopause. The PE distribution is fairly symmetric around the equa-

tor. Thus any asymmetry observed in TE distribution is mainly due to that of KE. The enhancement in both KE and PE over the tropical tropopause and in KE above the subtropical jet in the Northern Hemisphere is not seen for short-period waves (Fig. 6).

The values of PE decrease rapidly and monotonically as latitude increases in both hemispheres and become almost constant poleward of 30°. This latitudinal distribution of PE is consistent with a summer observation by Allen and Vincent (1995) using temperature data from the Australian radiosonde network.

The $R$ values are generally smaller than 1 at higher latitudes and decrease with latitude, which is similar to short-period waves. Large values of $R$ observed at high latitudes ($\phi > 60°$) may be meaningless since both KE and PE are small. Interestingly, $R$ is significantly greater than 1 around the tropical tropopause, where wave energy is maximized. This feature may be explained by the characteristics of equatorially trapped waves under an equatorial $\beta$-plane approximation. For equatorial Kelvin waves, $R$ is unity. For equatorial inertia-gravity waves, $R$ is greater than 1 and approaches unity as the zonal wavenumber and/or intrinsic wave frequency approaches infinity (see Sato and Dunkerton 1997). Thus, $R$ greater than 1 over the equator suggests that the small vertical-scale waves are a mixture including equatorial inertia-gravity waves.

Figure 9 shows latitude–height sections of $\overline{\Phi' w'}$, $\overline{u' w'}$, $\overline{v' w'}$, and EP flux divergence for small vertical-scale waves. Similar to short-period waves, energy flux in the stratosphere is upward except around the polar night jet. The distribution of the $\overline{u' w'}$ sign is also similar, but the distribution of its magnitude is different. Large negative values are observed above the subtropical westerly jets in both hemispheres. An interesting feature is the negative (positive) values of $\overline{v' w'}$ above the subtropical jet ($\sim$12 km) in the Northern (Southern) Hemisphere. This means equatorward propagation of gravity waves and is consistent with the statistical results shown by Sato (1994) based on the MU radar observation data over three years. This feature is not seen for short-period waves. The $\overline{v' w'}$ profile in the equatorial stratosphere suggests the dominance of poleward propagation from the equator, similar to short-period waves, but the magnitude is smaller. The EP flux divergence is decelerative above the subtropical jet also for small vertical-scale gravity waves. The magnitude is also comparable to that for short-period gravity waves.

#### 3) Difference between short-period and small vertical-scale gravity waves

It was clear that the two statistical characteristics do not necessarily accord. One distinct difference is that $\overline{v' w'}$ distributed in a V-shaped region with a center at the equator in the latitude–height section is larger for short-period waves than for small vertical-scale waves. This means that the short-period waves there have vertical wavelengths longer than 5 km. It may be hard to detect such long vertical wavelengths because radiosonde observations provide data for limited height ranges.

Another difference is the dominance of equatorward propagation over the subtropical jet seen only for small vertical-scale gravity waves. This suggests that the small vertical-scale waves there have periods longer than 1 day, and hence longer than the inertial period ($2\pi/f$) for $|\phi| > 30°$. It should be noted that the small vertical-scale gravity waves have large negative $\overline{u' w'}$ (Fig. 9), that is, a large westward component of their horizontal wavenumber vector. Periods of such gravity waves can be longer than the inertial period because of the Doppler effect of the strong subtropical jet, as seen in Fig. 4a. The Doppler effect is hard to estimate because it depends on wavenumbers as well as background winds. Thus it is difficult to extract gravity waves from only their frequencies.

These differences suggest that we have to be careful in interpreting observational statistics because observations account for only a part of gravity waves distributed in a wide spectral range of frequency and wavenumbers.

## 6. Discussion

### *a. Meridional propagation of internal inertia-gravity waves*

The energy of gravity waves was largest in the equatorial region and was distributed in a wide spectral range of frequency as shown in Figs. 4 and 5. The latitude–height section of $\overline{v' w'}$ shown in Figs. 7c and 9c suggested that gravity waves propagate poleward from the equatorial region.

The meridional propagation of each gravity wave depends on the wave parameters describing its structure. The dispersion relation for an inertia-gravity wave is

$$\hat{\omega}^2 = \frac{f^2 m^2 + (k^2 + l^2) N^2}{m^2 + k^2 + l^2}, \tag{8}$$

where $\hat{\omega}$ is the intrinsic wave frequency and $m$, $k$, and $l$ are vertical, zonal, and meridional wavenumbers, respectively (Gill 1982). The elevation angle $\theta$ of the inertia-gravity wave ray in the latitude–height section is expressed as

$$\tan\theta = \frac{C_{gz}}{C_{gy}} = \frac{\partial\hat{\omega}/\partial m}{\partial\hat{\omega}/\partial l} = \sqrt{\frac{k^2 + l^2}{l^2}} \sqrt{\frac{\hat{\omega}^2 - f^2}{N^2 - \hat{\omega}^2}}. \tag{9}$$

The angle $\theta$ is smallest for the gravity waves propagating meridionally ($k = 0$). The intrinsic frequency $\hat{\omega}$ of meridionally propagating gravity waves is almost the same as ground-based frequency $\omega$ ($\equiv \hat{\omega} + Vl$), because the background meridional wind $V$ is weak. Equation (9) indicates that as the wave frequency $\hat{\omega}$ is lower, the angle $\theta$ is smaller. In other words, lower-frequency

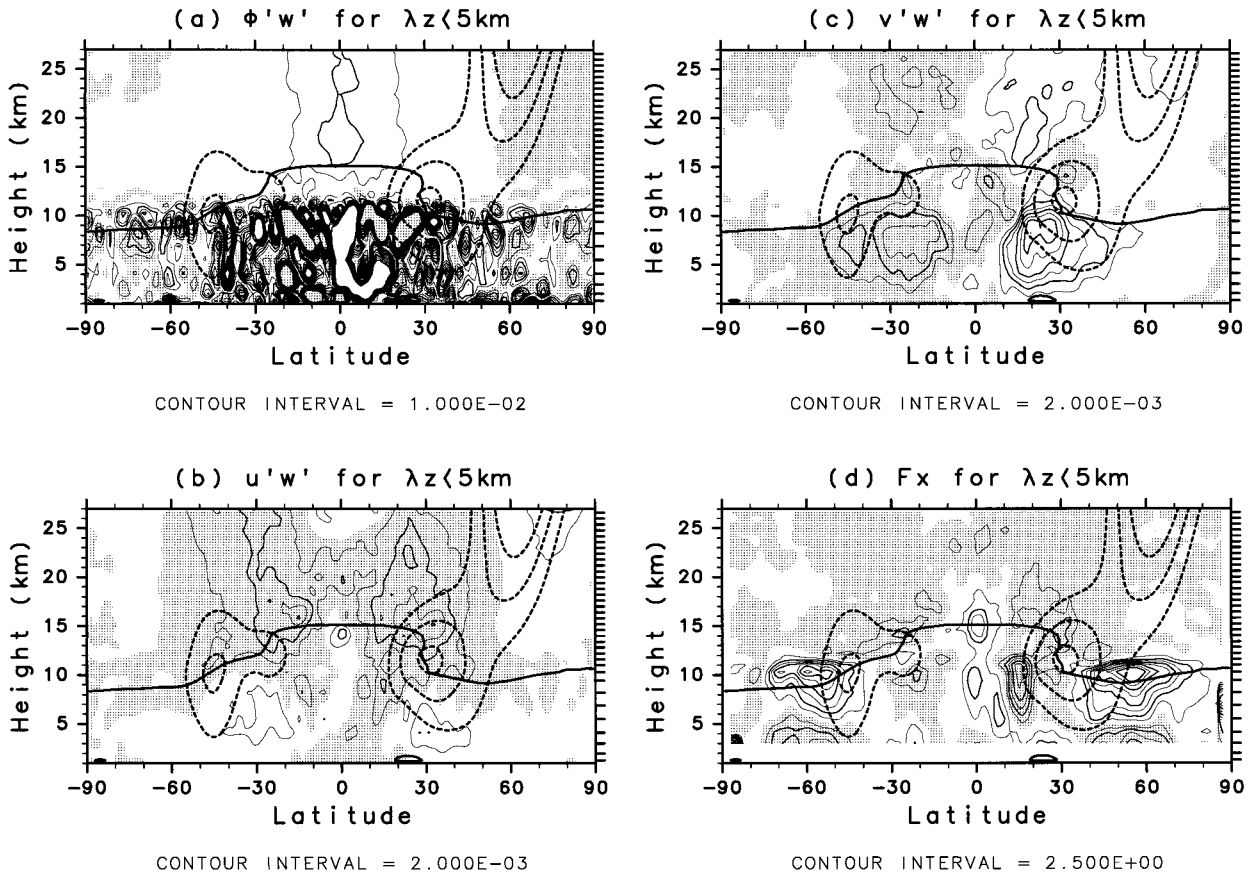


FIG. 9. The same as Fig. 7 but for small vertical-scale gravity waves.

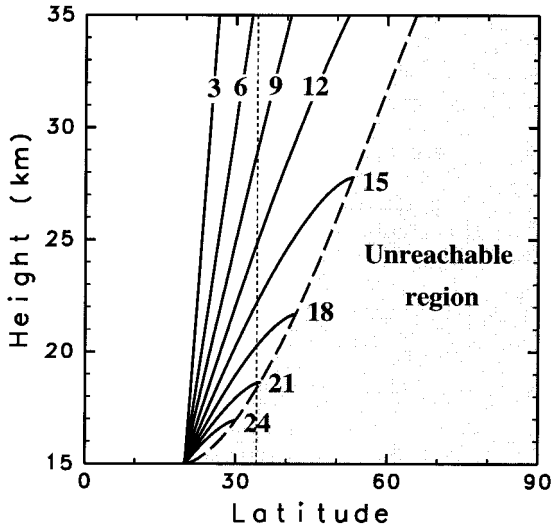


FIG. 10. Rays of poleward propagating inertia-gravity waves that pass through $\phi = 20°$ at a height of 15 km. Numbers near each ray denote the wave period in hours. The region where the inertia-gravity waves cannot reach is shaded. A thin dashed line indicates $\phi = 34.2°$.

gravity waves from the equatorial region should be observed at lower altitudes in off-equatorial regions. Here we should note that the gravity waves cannot propagate beyond the latitude at which the intrinsic wave frequency equals the inertial frequency, as explained in the next section.

This point is illustrated by Fig. 10, which shows the ray paths obtained by integrating their group velocities for gravity waves with $k = 0$ passing through the tropopause of 15 km at $\phi = 20°$. This latitude was chosen because the $\overline{v'w'}$ contours of $\pm 2 \times 10^{-3}$ m$^2$ s$^{-2}$ are located there in Fig. 7c. The Doppler effect of the mean meridional wind is ignored. Numbers on each ray denote the wave period in hours. In Fig. 10 the region where gravity waves from the equatorial region cannot reach is shaded.

Several features observed in the momentum fluxes and spectra of gravity waves shown in sections 4 and 5 are explained by the poleward propagation of gravity waves generated in the equatorial region. Large $\overline{v'w'}$ values are distributed in a V-shaped region over the equatorial region. The boundary of this V-shaped region is almost in accord with the boundary of unreachable region traced by a dashed curve in Fig. 10. For example, both boundaries are located at $z \sim 21$ km for $|\phi| = 40°$ and $z \sim 26$ km for $|\phi| = 50°$.

Figure 10 suggests also that the meridionally propagating gravity waves with near-inertial frequencies should be observed at the lowest altitudes in the off-equatorial region among gravity waves propagating from the equatorial region. For example, at the latitude of 34.2°, the gravity waves having a near-inertial period of 21 h should be observed at $z = 19$ km. This is consistent with the power spectra as a function of height (Fig. 3b). Gravity waves with near-inertial frequency (but having zonal component of wavevector $k$) and those with higher frequencies have larger elevation angles of the rays. Hence, they should be observed at higher altitudes. The frequency bandwidth of gravity wave spectra must then increase with height, which is also consistent with the feature observed in Fig. 3b. For example, the waves with the period of 12 h are observed above $z = 25$ km, as suggested by Fig. 10.

### b. *Dominance of gravity waves with near-inertial frequency*

The frequency spectra as a function of latitude shown in Figs. 4 and 5 indicated that gravity waves having near-inertial frequency are dominant at every latitude except for the equatorial region. Such an enhancement of energy near the inertial frequency in the lower stratosphere is reported by a few observational studies (Thompson 1978; Nastrom et al. 1997) as well as Sato et al. (1997).

One explanation for the dominance of near-inertial frequency waves is the meridional propagation of gravity waves generated in the equatorial troposphere, as discussed in section 6a. The vertical group velocity $C_{gz}$ is expressed as

$$C_{gz} = -\frac{2m(\hat{\omega}^2 - f^2)}{m^2 + k^2}, \tag{10}$$

and the horizontal group velocity $\mathbf{C}_{gh}$ is expressed as

$$\mathbf{C}_{gh} = \frac{2m^2(\hat{\omega}^2 - f^2)}{(m^2 + k^2)k}\frac{\mathbf{k}}{|k|} + \mathbf{U}, \tag{11}$$

where $\mathbf{k}$ is the horizontal wavenumber vector (not necessarily zonal) and $\mathbf{U}$ is the mean wind velocity. When the intrinsic frequency $\hat{\omega}$ approaches $f$, both vertical and horizontal group velocities (relative to the mean wind) become zero (Jones 1967). Thus, if the gravity waves propagate poleward and reach its critical latitude where $\hat{\omega} = f$, the energy of gravity waves may be accumulated there and observed as an isolated peak near-inertial frequency at one location, as in Fig. 3.

Another explanation is related to the wave vertical propagation in the mean wind having vertical shear. The ground-based frequency $\omega$ of a gravity wave is conserved in a steady mean wind, and the intrinsic frequency $\hat{\omega}$ (taken to be positive without losing generality) is modified by the mean wind:

$$\hat{\omega} = \omega - \mathbf{U}\cdot\mathbf{k}. \tag{12}$$

Over the subtropical westerly jet, $\overline{u'w'}$ was negative, suggesting that zonal wavenumbers of dominant gravity waves are negative. Thus, for gravity waves propagating upward in the negative vertical shear above the subtropical westerly jet, $\hat{\omega}$ decreases with height and may encounter the critical level where $\hat{\omega} = f$. For this given situation, the critical level is lower for gravity waves having smaller $\omega$. This inference is consistent with the vertical structure of power spectra shown in Fig. 3b. Here the frequency of the spectral peak above 16 km increases with height and approaches the inertial frequency at 23 km where $U$ becomes almost zero (see Fig. 2c). Equation (11) shows that a gravity wave whose $\omega$ is near $f$ has almost zero group velocity in the weak mean wind and is prone to stay there, keeping their wave structure and energy. Such a gravity wave may be seen as a clear isolated peak in the frequency spectra at one location, as in Fig. 3. This explanation is also in agreement with the westward propagation of gravity waves with near-inertial frequencies observed in the MU radar data of Figs. 2a and 2b (Sato et al. 1997). It will be important to examine the phase structure of the gravity waves with near-inertial frequencies in future work.

### c. *Downward propagation of gravity waves in the polar region*

An interesting feature in our model is the dominance of downward energy propagation around the polar night jet (Figs. 7a and 9a), although energy propagation of gravity waves is mostly upward in the tropical and midlatitude regions. There have been few observational studies of gravity waves in the polar region except for a few concerning mountain waves. Although a Rayleigh friction is used in our model to damp wave amplitudes near the top layer, some reflection of gravity waves may occur there. However, it should be emphasized that gravity waves propagating energy downward can exist in the real atmosphere.

First, the gravity waves can be reflected in the real atmosphere. From the dispersion relation (8) for an inertia-gravity wave, $m$ is expressed as

$$m^2 = \frac{N^2 - \hat{\omega}^2}{\hat{\omega}^2 - f^2}k^2, \tag{13}$$

$$= \frac{(N^2/k^2) - (c - U)^2}{(c - U)^2 - (f^2/k^2)}k^2, \tag{14}$$

where $c$ is the horizontal phase velocity and $U$ is the background wind parallel to the horizontal wavenumber vector **k.** The phase velocity $c$ is invariant if the background wind is steady and uniform in the direction of the horizontal wavenumber vector. Nonzero $\overline{u'w'}$ values in the polar region in Figs. 7b and 9b indicate that gravity waves have nonzero zonal wavenumbers. When such gravity waves propagate poleward and encounter the strong polar night jet, $(c - U)^2$ may become larger than $N^2/k^2$. In this case, $m^2$ becomes negative so that

the gravity waves are reflected there in the strong polar night region. The features in Figs. 7a and 9a showing that the downward energy fluxes are larger in the northern polar stratosphere than in the Southern Hemisphere are consistent with this inference.

Second, the gravity waves may be generated in situ around the polar night jet. According to observations, gravity waves are generated around the subtropical jet and propagate energy upward and downward from the jet core (Hirota and Niki 1986; Sato 1994). The upward propagating gravity waves were observed in our model in the stratosphere. These gravity waves are considered to be generated through the geostrophic adjustment around unbalanced flow. A similar generation mechanism of gravity waves may also act around the polar night jet. To confirm the existence of gravity waves propagating downward around the polar night jet, observational studies are necessary.

## 7. Summary and concluding remarks

Using a high-resolution GCM (T106L53), global distribution and characteristics of gravity waves were examined. The horizontal resolution was roughly equivalent to 120-km grid spacing and the vertical spacing in the upper troposphere and lower stratosphere was 600 m. The bottom boundary condition was the same as for an aquaplanet with perpetual February SST independent of longitude. Monochromatic gravity waves that appeared in the midlatitude lower stratosphere of the model were similar to the MST radar observations in terms of wave period, vertical wavelength, and amplitudes. The spectral characteristics were also in accord with the observation. This fact suggests that the gravity waves simulated in the model are fairly realistic.

The frequency spectra were examined as a function of latitude. At higher latitudes ($>10°$), a significant peak is observed near the inertial frequency in the lower stratosphere. On the other hand, the spectra are distributed in a wide range of frequency over the equator in which the inertial frequency is zero. Two possible explanations were discussed for the peak near the inertial frequency. One attributed the peak to the meridional propagation of gravity waves from the equatorial region, and the other was attributed to the vertical propagation of gravity waves whose intrinsic frequency approaches the inertial frequency.

Two kinds of gravity wave components in the stratosphere were extracted using a highpass filter in time and height as usually done in observational studies. Both kinds of waves propagated mostly upward and westward. Meridional propagation of short-period waves was poleward from the equatorial region. The wave energy reaches 50° lat at 27-km altitude, which is consistent with theoretical characteristics of inertia-gravity waves. Small vertical-scale waves propagated equatorward over the subtropical jet, which was consistent with observations. The latitudinal distribution of potential energy was also similar to observational statistics. The ratio of potential to kinetic energy was maximized over the equator, then decreased with latitude up to $\phi \sim \pm 30°$, and became almost constant at higher latitudes. The EP flux divergence is decelerative above the subtropical jet for both kinds of gravity waves, although it is weak.

In the equatorial region, poleward and upward propagation of gravity waves as observed in our model may be modified by the QBO. Using a three-dimensional mechanistic model (T42) in which localized heating is put in the tropical region, Horinouchi and Yoden (1997) recently discussed meridional propagation of gravity waves from the equatorial region as modulated by the QBO in the equatorial lower stratosphere. The results of our study suggest that the QBO signal may be observed, even in the middle latitude lower stratosphere.

By using the subsets of the huge amount of data obtained with this high-resolution GCM simulation, further interesting examinations are possible: three-dimensional structure of gravity waves having near-inertial frequency in the stratosphere, the generation and interaction with synoptic-scale baroclinic waves of gravity waves that are dominant above the subtropical jet, and the possible role of small-scale gravity waves on the QBO in the equatorial stratosphere.

With the aid of computer technology development, the role of GCMs that can resolve small-scale phenomena and incorporate detailed processes of radiation and photochemistry may become more and more important to the study of atmospheric circulation. It is important, however, that observation and model studies are complementary. To confirm new features obtained from GCMs such as downward propagating gravity waves in the polar region, observational support is necessary.

*Acknowledgments.* One of the authors (KS) thanks S. Yoden for a fruitful discussion. Thanks are also due to S. D. Eckermann, I. Hirota, M. E. McIntyre, T. Satomura, R. A. Vincent, and the anonymous reviewers for their constructive comments. This study was supported by Center for Climate System Research of the University of Tokyo, partly by a Grant-in-Aid for Scientific Research (A) (2)08404026 (KS) and (B) 06452083 (MT) of the Ministry of Education, Science and Culture, Japan, and by International Cooperative Study of Stratospheric Change and its Role in Climate from the Science and Technology Agency of Japan (TK). Partial calculation of the low resolution model was made by KDK (Kyoto daigaku Denpakagaku Keisanki-jikken souchi) of Radio Atmospheric Science Center (RASC) at Kyoto University. The MU radar belongs to and is operated by RASC. The GFD-DENNOU library was used for drawing figures.

## REFERENCES

Alexander, M. J., 1998: Interpretations of observed climatological patterns in stratospheric gravity wave variance. *J. Geophys. Res.*, in press.

——, and K. Rosenlof, 1996: Nonstationary gravity wave forcing of the stratospheric zonal mean wind. *J. Geophys. Res.,* **101,** 23 465–23 474.

Allen, S. J., and R. A. Vincent, 1995: Gravity wave activity in the lower atmosphere: Seasonal and latitudinal variations. *J. Geophys. Res.,* **100,** 1327–1350.

Andrews, D. G., J. R. Holton, and C. B. Leovy, 1987: *Middle Atmosphere Dynamics.* Academic Press, 489 pp.

Dunkerton, T. J., 1997: The role of gravity waves in the quasi-biennial oscillation. *J. Geophys. Res.,* **102,** 26 053–26 076.

Eckermann, S. D., I. Hirota, and W. K. Hocking, 1995: Gravity wave and equatorial wave morphology of the stratosphere derived from long-term rocket soundings. *Quart. J. Roy. Meteor. Soc.,* **121,** 149–186.

Fetzer, E. J., and J. C. Gille, 1994: Gravity wave variance in LIMS temperatures. Part I: Variability and comparison with background winds. *J. Atmos. Sci.,* **51,** 2461–2483.

Fukao, S., T. Sato, T. Tsuda, S. Kato, K. Wakasugi, and T. Makihira, 1985: The MU radar with an active phased array system. Part 1: Antenna and power amplifiers. *Radio Sci.,* **20,** 1155–1168.

Gill, A. E., 1982: *Atmosphere–Ocean Dynamics.* Academic Press, 662 pp.

Hamilton, K., 1996: Comprehensive meteorological modelling of the middle atmosphere: A tutorial review. *J. Atmos. Terr. Phys.,* **58,** 1591–1627.

Hayashi, Y., D. G. Golder, J. D. Mahlman, and S. Miyahara, 1989: The effect of horizontal resolution on gravity waves simulated by the GFDL ''SKYHI'' general circulation model. *Pure Appl. Geophys.,* **130,** 421–443.

——, ——, and P. W. Jones, 1997: Tropical gravity waves and superclusters simulated by high-horizontal-resolution SKYHI general circulation models. *J. Meteor. Soc. Japan,* **75,** 1125–1139.

Haynes, P. H., and J. Anglade, 1997: The vertical-scale cascade in atmospheric tracers due to large-scale differential advection. *J. Atmos. Sci.,* **54,** 1121–1136.

Hirota, I., 1984: Climatology of gravity waves in the middle atmosphere. *J. Atmos. Terr. Phys.,* **46,** 767–773.

——, and T. Niki, 1986: Inertia-gravity waves in the stratosphere. *J. Meteor. Soc. Japan,* **64,** 995–999.

Horinouchi, T., and S. Yoden, 1997: Propagation of waves excited by localized episodic heating in the Tropics and their effect on the middle atmosphere: Comparison between two QBO phases. *J. Meteor. Soc. Japan,* **75,** 641–656.

——, and ——, 1998: Wave–mean flow interaction associated with a QBO-like oscillation in a simplified GCM. *J. Atmos. Sci.,* **55,** 502–526.

Iwasaki, T., S. Yamada, and K. Tada, 1989: A parameterization scheme of orographic gravity wave drag with two different vertical partitionings. Part I: Impacts on medium-range forecasts. *J. Meteor. Soc. Japan.,* **67,** 11–27.

Jones, W. L., 1967: Propagation of internal gravity waves in the fluids with shear and rotation. *J. Fluid Mech.,* **30,** 439–448.

Jones, W. P., K. Hamilton, and R. J. Wilson, 1997: A very high resolution general circulation model simulation of the global circulation in austral winter. *J. Atmos. Sci.,* **54,** 1107–1116.

Kitamura, Y., and I. Hirota, 1989: Small-scale disturbances in the lower stratosphere revealed by daily rawinsonde observations. *J. Meteor. Soc. Japan,* **67,** 817–831.

Lindzen, R. S., 1981: Turbulence and stress due to gravity wave and tidal breakdown. *J. Geophys. Res.,* **86,** 9707–9714.

Manzini, E., and K. Hamilton, 1993: Middle atmospheric traveling waves forced by latent and convective heating. *J. Atmos. Sci.,* **50,** 2180–2200.

Matsuno, T., 1982: A quasi one-dimensional model of the middle atmosphere circulation interacting with internal gravity waves. *J. Meteor. Soc. Japan,* **60,** 215–226.

McFarlane, N. A., 1987: The effect of orographically excited gravity wave drag on the general circulation of the lower stratosphere and troposphere. *J. Atmos. Sci.,* **44,** 1775–1880.

Nakajima, T., M. Tsukamoto, Y. Tsusima, and A. Numaguti, 1995: Modeling of the radiative process in a AGCM. Reports of a new program for creative basic research studies. *Studies of Global Environment Change with Special Reference to Asia and Pacific Regions,* T. Matsuno, Ed., Vol. I-3, Center for Climate System Research, University of Tokyo, 104–123.

Nastrom, G. D., T. E. vanZandt, and J. M. Warnock, 1997: Vertical wavenumber spectra of wind and temperature from high resolution balloon soundings over Illinois. *J. Geophys. Res.,* **102,** 6685–6701.

Numaguti, A., 1993: Dynamics and energy balance of the Hadley circulation and the tropical precipitation zones: Significance of the distribution of evaporation. *J. Atmos. Sci.,* **50,** 1874–1887.

——, M. Takahashi, T. Nakajima, and A. Sumi, 1995: Development of an atmospheric general circulation model. Reports of a new program for creative basic research studies. *Studies of Global Environment Change with Special Reference to Asia and Pacific Regions,* T. Matsuno, Ed., Vol. I-3, Center for Climate System Research, University of Tokyo, 1–27.

O'Sullivan, D., and T. J. Dunkerton, 1995: Generation of inertia-gravity waves in a simulated life cycle of baroclinic instability. *J. Atmos. Sci.,* **52,** 3695–3716.

Palmer, T. N., G. J. Shutts, and R. Swinbank, 1986: Alleviation of a systematic westerly bias in general circulation and numerical weather prediction models through an orographic gravity wave drag parameterization. *Quart. J. Roy. Meteor. Soc.,* **112,** 1001–1040.

Sato, K., 1994: A statistical study of the structure, saturation and sources of inertia-gravity waves in the lower stratosphere observed with the MU radar. *J. Atmos. Terr. Phys.,* **56,** 755–774.

——, and T. J. Dunkerton, 1997: Estimates of momentum flux associated with equatorial Kelvin and gravity waves. *J. Geophys. Res.,* **102,** 26 247–26 261.

——, D. J. O'Sullivan, and T. J. Dunkerton, 1997: Low-frequency inertio-gravity waves in the stratosphere revealed by three-week continuous observation with the MU radar. *Geophys. Res. Lett.,* **24,** 1739–1742.

Takahashi, M., 1996: Simulation of the stratospheric quasi-biennial oscillation using a general circulation model. *Geophys. Res. Lett.,* **23,** 661–664.

——, N. Zhao, and T. Kumakura, 1997: Equatorial waves in a general circulation model simulating a quasi-biennial oscillation. *J. Meteor. Soc. Japan,* **75,** 529–540.

Thompson, R. O. R. Y., 1978: Observation of inertial waves in the stratosphere. *Quart. J. Roy. Meteor. Soc.,* **104,** 691–698.

Tsuda, T., Y. Murayama, M. Yamamoto, S. Kato, and S. Fukao, 1990: Seasonal variation of momentum flux in the mesosphere observed with the MU radar. *Geophys. Res. Lett.,* **17,** 725–728.

Wu, D. L., and J. W. Waters, 1996: Satellite observations of atmospheric variances: A possible indication of gravity waves. *Geophys. Res. Lett.,* **23,** 3631–3634.